An adaptive non-raster scanning method in atomic force microscopy for simple sample shapes

OPEN ACCESS
IOP Publishing
Measurement Science and Technology
Meas. Sci. Technol. **26** (2015) 035401 (12pp)
doi:10.1088/0957-0233/26/3/035401

An adaptive non-raster scanning method in atomic force microscopy for simple sample shapes

Kaiqiang Zhang[1], Toshiaki Hatano[1], Thang Tien[2], Guido Herrmann[1], Christopher Edwards[2], Stuart C Burgess[1] and Mervyn Miles[3]

[1] Department of Mechanical Engineering, University of Bristol, University Walk, BS8 1TR, UK
[2] Engineering Department, University of Exeter, UK
[3] School of Physics, University of Bristol, UK

E-mail: g.herrmann@bris.ac.uk

Received 25 September 2014, revised 20 November 2014
Accepted for publication 19 January 2014
Published 16 February 2015

Abstract

It is a significant challenge to reduce the scanning time in atomic force microscopy while retaining imaging quality. In this paper, a novel non-raster scanning method for high-speed imaging is presented. The method proposed here is developed for a specimen with the simple shape of a cell. The image is obtained by scanning the boundary of the specimen at successively increasing heights, creating a set of contours. The scanning speed is increased by employing a combined prediction algorithm, using a weighted prediction from the contours scanned earlier, and from the currently scanned contour. In addition, an adaptive change in the height step after each contour scan is suggested. A rigorous simulation test bed recreates the x–y specimen stage dynamics and the cantilever height control dynamics, so that a detailed parametric comparison of the scanning algorithms is possible. The data from different scanning algorithms are compared after the application of an image interpolation algorithm (the Delaunay interpolation algorithm), which can also run on-line.

Keywords: non-raster scanning, atomic force microscopy, boundary contour scan, contour prediction, image interpolation

(Some figures may appear in colour only in the online journal)

1. Introduction

In atomic force microscopy (AFM), the interaction force is an important measure of the distance between a sharp tip-cantilever and the sample profile [7]. This facilitates the control of the cantilever height so that the cantilever remains above the specimen. Generally, the tip is controlled to follow a rectangular scanning raster in the x–y plane to cover the substrate. In this way, the topography of the scanned specimen-substrate is constructed along the raster. The use of a raster scanning approach has been a general feature of many recently developed high-speed force microscopy systems as outlined in [4, 9], pushing the speed of some of the most advanced force microscopes well above the level of 10 frames per second: e.g. a set-up providing 1000 frames per second, exploiting as much as possible the mechanical stability and linearity of the design, and avoiding any closed loop control, is described in [9] (and the references therein). Nevertheless, many AFMs focus on closed-loop control, for example to minimize forces associated with the specimen-cantilever interaction [28].

AFMs have been widely used in practical material studies and biological research (e.g. [21, 31]). This has also led to detailed theoretical and numerical analysis of the relative effect of the tip/sample shape on imaging quality, for instance tip-dilation/radius [12, 22, 30], and relevant algorithms for sample image recovery [30]. The analysis and simulation

results for the measurement algorithms proposed originally in [12] were subsequently practically verified in [13]. Despite these advances, the imaging time using a raster scanning method, in particular in commercial AFMs, can often take several seconds. Real-time dynamic changes in the specimen cannot necessarily be observed within extended scanning time intervals. As an alternative to raster scanning, optimal tip trajectory approaches have been suggested, which are similar to, but more efficient than, typical raster scanning, e.g. [33]. Moreover, novel control methods for the tip-cantilever interaction have been developed: for example, for the vibration control of the tip-cantilever to be tested in simulation [32]. However, these scanning approaches require accuracy and high bandwidth in the vertical tip-cantilever control loop, while driving the tip along the sample surface at high-speed [1]. Furthermore, unavoidable excitations of the tip-cantilever dynamics introduce noise into the imaging data and the sharp tip may damage the sample.

In general, scanning algorithms in AFM applications 'explore' a fixed scanning area while ignoring local information from the collected data. Hence, scanning may involve significant 'wasted' time while the tip travels the entire substrate—including possibly specimen-irrelevant areas. In contrast, some of the first ideas for non-raster scans were suggested by Marinello *et al* [19], where simple specimens were scanned along free paths or contours on the specimen. An alternative non-raster scanning algorithm was developed by Andersson [3, 10, 11, 15] utilizing a feedback methodology, which considers collected information and relevant path prediction during the scanning. However, for the work in [3, 10, 11, 15], the non-raster scanning algorithm, also called local raster scanning, is mainly designed for string-like samples, e.g. DNA. Thus, the scanning path tends to cross the sample to follow the topology of the sample. This may not be always desirable, as the cantilever may damage in particular biological specimens [20], or else the cantilever specimen interaction can introduce undesirable dynamics which will invalidate the scanning results [2, 20]. One solution is a lower Q-factor to reduce dynamic effects [2]. However, this will certainly slow down the scanning speed [4] and may increase the necessary force interaction [2]. Thus, minimal interaction of the cantilever with the specimen is a highly desirable target.

Considering the initial ideas of [19] and the above limitations of the predictive feedback based algorithms by Andersson [3, 10, 11, 15], we suggest in this paper a novel scanning approach for specimens of fairly simple structure, e.g. cells, which are smooth and have neither links nor cross points on their contours. The topography of such a sample can be constructed from surface contours at different heights, i.e. we can image a simple object sample by scanning its smooth contours, which are closed curves in the plane. This is inspired and similar to methods such as [19] or [6],[4] but in contrast to such methods, here we seek minimal interaction with the specimen, and in particular we wish to avoid crossing the specimen. Considering these ideas, the contributions in this paper are

(a) Extending Andersson's non-raster scanning for string-like samples [11], whereby the original sinusoid-based tip trajectory is modified so that the trajectory does not cross the specimen, creating a piece-wise sine/cosine trajectory (section 2) designed to remain within the sample vicinity.
(b) The direction of motion of the new sine/cosine trajectory is determined by a combined prediction method (section 3). It uses an estimated curve model of the currently scanned contour for one part of the combined estimation. In addition, it develops an alternative model by exploiting the similarity of nearby boundary contours at different heights. Hence, we consider a weighted average of these two models. With the proposed curve model prediction, the tip can be controlled to remain in the vicinity of the specimen avoiding the scanning of areas of less interest. Most importantly, the cantilever tip height remains fixed while scanning for one boundary contour, i.e. the tip height changes only when scanning for a higher boundary contour. Hence, the complexity of the controller reduces, relying on a high speed x–y-specimen stage control.
(c) The trajectory prediction model is, in addition, used to adaptively decrease the amplitude of the piece-wise sine/cosine trajectory once the prediction model shows greater reliability (section 3). An argument for stability of the overall algorithm is also given.
(d) Another novel element is a new predictive mechanism for the cantilever height controller, which facilitates increasing the cantilever height step between boundary scans, in the situation in which the specimen shows a steep slope (section 4).
(e) A detailed simulation environment for the cantilever height control and the x–y stage positioning has been developed to allow a realistic comparison of the raster scanning and the different non-raster scanning algorithms (section 6).
(f) Inspired by the ideas in [15], a fast, real-time implementable Delaunay interpolation algorithm is introduced to reconstruct the image using samples from the non-raster algorithm, and a direct error with respect to the original specimen can be computed (section 5), which permits a detailed parametric comparison between the algorithms.

In this sense, here we advance our previous work in [34] to a more practically relevant setting (item (e), above), by utilizing the image interpolation algorithm (item (f)), by providing a detailed practical parameter study, and by introducing additional ideas (item (d), above), which enhance the scanning in areas where the specimen has only a moderate slope.

2. Andersson's non-raster scanning method and a trajectory for object samples

In this work, we focus on simple specimens, like cells. For such a sample, the contour can be modelled as a solid, smooth

[4] Note that the robotics inspired work of [6] can be powerful as it can produce good contour scanning results once the correct control gains are found, exploiting some sufficient conditions. However, the contour scans may cause cantilever specimen interaction, as there is no direct guarantee that the cantilever tip crosses the specimen: this contrasts with the work presented here.

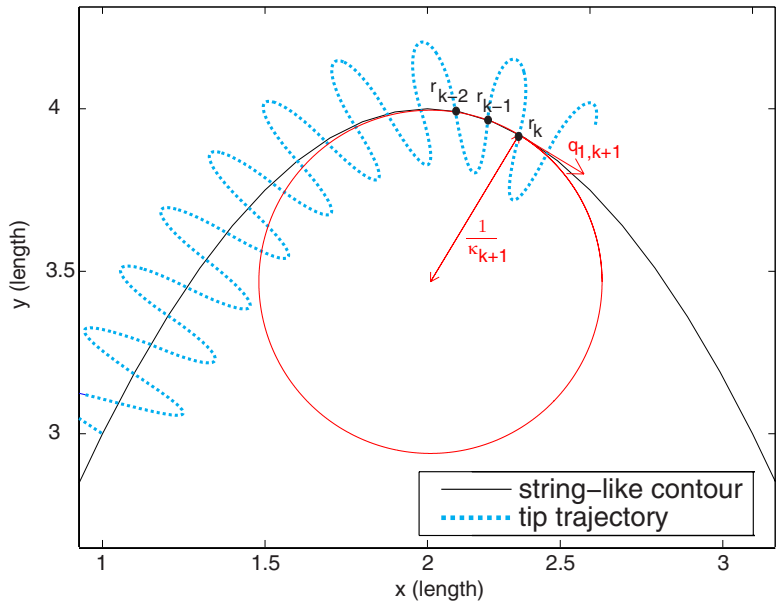

Figure 1. An illustration of Andersson's non-raster scanning algorithm with smooth trajectory and contour prediction.

boundary at one height. Therefore, we consider the basic idea and the curve estimation schemes of Andersson's non-raster scanning method in [3, 10, 11, 15] as the starting point for our proposed algorithm.

At any fixed height, the contour for a string-like, continuous specimen (e.g. DNA) or the continuous, smooth boundary of a specimen can be modelled as a curve in a plane. Thus, the spatial evolution of the contour can be given in the Frenet–Serret frame [3] by

$$\frac{\mathrm{d}r(s)}{\mathrm{d}s} = q_1(s)\,, \tag{1a}$$

$$\frac{\mathrm{d}q_1(s)}{\mathrm{d}s} = \kappa(s)q_2(s), \tag{1b}$$

$$\frac{\mathrm{d}q_2(s)}{\mathrm{d}s} = -\kappa(s)\,q_1(s), \tag{1c}$$

where $r(s)$ stands for the position vector in the fixed frame with arclength s on the curve, $q_1(s)$ is the tangent vector at the point, $q_2(s)$ is the normal vector with respect to point $r(s)$ and $\kappa(s)$ is the curvature at point $r(s)$. The arclength variable s is a function of time t. The function $s(t)$ is defined for the scanning process through a desired scan velocity.

In recent non-raster scanning methods, the tip motion trajectory is determined by a prediction using data associated with the current contour scan. Practically, the tip is moved along smooth sine segments around the estimated curve (see figure 1). During one boundary scan, the estimation of the curvature and the tangent of the curve is updated with each triple of newly obtained points r_k, r_{k-1}, and r_{k-2} on the curve in real-time. Here r_k stands for the kth measured point on the curve in the Cartesian coordinates frame. Assuming a very small arclength difference in s between each two adjacent points on the boundary, the curvature and tangent at point r_k is approximated from r_k, r_{k-1}, and r_{k-2}. Therefore, the k+1th curve 'states' can be estimated from the data at the kth step. For the heading direction of the current tip motion, the tangent vector $q_{1,k+1}$ and normal vector $q_{2,k+1}$ approximately satisfy [3]

$$q_{1,k+1} = \frac{r_{k-1} - r_k}{r_{k-1} - r_k}, q_{2,k+1} = \begin{bmatrix} 0 & -1 \\ 1 & 0 \end{bmatrix} q_{1,k+1}\,. \tag{2}$$

Here the Euclidean distances, $d(\cdot,\cdot)$, between each of the two points selected from r_{k-2}, r_{k-1}, and r_k are $a = d\,(r_{k-2}, r_{k-1})$, $b = d(r_{k-1}, r_k)$ and $c = d(r_{k-2}, r_k)$ (see figure 1). Based on Heron's formula [3], the curvature estimation for the k+1th sample is given by

$$\kappa_{k+1} = \pm 4\sqrt{\frac{\ell\,(\ell - a)\,(\ell - b)\,(\ell - c)}{abc}}, \ell = \frac{1}{2}\,(a + b + c)\,, \tag{3}$$

where κ_{k+1} is the k+1th curvature estimation. When the cosine of the angle between the vector (r_{k-1}, r_k) and the normal vector is positive, the κ_{k+1} takes positive sign. Otherwise, κ_{k+1} is negative.[5]

Building on Andersson's smooth trajectory [11], a novel trajectory is introduced in figure 2, which is constructed in two parts: (*a*) a sine-curve to send the tip towards the sample contour to allow the measuring of points on the contour; (*b*) a cosine-curve to move away from the contour, thus, avoiding the crossing of the sample when a point on the contour is measured. For any instant s_1, s_2, …, where $r_d(s_i)$ describes a point on the contour, the tip trajectory is defined by

$$r_t(s - s_i) = r_t(s - s_i) = \begin{cases} r_d\,(s - s_i) + \dfrac{A}{2}\,(1 - \cos\,(2\omega\,(s - s_i))\,)\,q_2\,(s - s_i)\,, \\ \qquad\qquad \text{for } 0 \le s - s_i \le \dfrac{\pi}{2\omega} \\ r_d\,(s - s_i) + A\sin\,(\omega\,(s - s_i))\,q_2\,(s - s_i)\,, \\ \qquad\qquad \text{for } \dfrac{\pi}{2\omega} \le s - s_i \end{cases} \tag{4}$$

for $s - s_i \ge 0$. Here, the parameter, A, denotes the amplitude of the scanning trajectory, ω is the spatial frequency of the

[5] Measurement noise might be amplified: Here a Kalman filter is recommended to reduce the noise influence (see Andersson [7]).

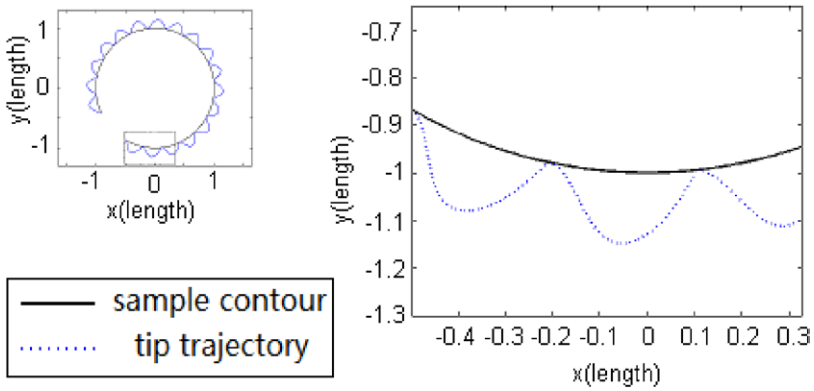

Figure 2. Example of the proposed trajectory. Here the curvature of the target contour is constant, while $A = 0.2$, and $\omega = 0.1$.

trajectory, and q_2 is the normal vector to the contour. The symbol r_d indicates the estimated contour position and r_t is the demanded cantilever tip position as a function of arclength s. Thus, the two parts of the trajectory are smooth and continuously joined at the point $s - s_i = \pi / 2\omega$. Moreover, the tangent of the scanning trajectory coincides with the contour tangent for $s \to s_i+$, which avoids crossing into the specimen and introduces the least possible change in tangent at $s = s_i$.

The performance of the proposed scanning trajectory is influenced by the amplitude A and the spatial frequency ω. This is similar to Chang and Andersson [10, 11], who point out, that A determines the search region of the trajectory, and the trajectory is guaranteed to measure a point on the contour for large enough A. Moreover, a large value for ω implies a high density of points along the contour in the current scan.

Practically, the tip needs to be controlled with respect to time t. To derive a function $s(t)$, we propose a constant tip velocity $v_{tip} = \mathrm{d}r_{tip} / \mathrm{d}t$ to ensure the trajectory is as smooth as possible, thus avoiding the excitation of the dynamics in the cantilever-tip system and the actuators. Considering the time derivative of the tip position in the Frenet–Serret frame and the requirement for a constant tip velocity $\| v_{tip} \| = \text{const}$, we compute from (4) and (1)

$$\| v_{tip} \| = \| \frac{\mathrm{d}r_{tip}(t)}{\mathrm{d}t} \| = f(s) \frac{\mathrm{d}s}{\mathrm{d}t}, \tag{5}$$

where the function $f(s)$ is defined as

$$f(s) = \begin{cases} \sqrt{\left(1 - \frac{A}{2}\kappa - \frac{A}{2}\kappa\cos(2\omega(s - s_i))\right)^2 + (A\omega\sin(2\omega s))^2} \\ \quad \text{for } 0 \le s(t) - s_i \le \frac{\pi}{2\omega} \\ \sqrt{(1 - A\kappa\sin(\omega(s - s_i)))^2 + (A\omega\cos(\omega(s - s_i)))^2} \\ \quad \text{for } \frac{\pi}{2\omega} \le s - s_i \end{cases},$$

so that $\| v_{tip} \| \mathrm{d}t = f(s)\ \mathrm{d}s$. Under the assumption of constant tip velocity, the relationship between s and t is calculated by an integral operation according to $\| v_{tip} \| t = \int_0^s f(\rho)\mathrm{d}\rho$. This permits the calculation of arclength s as a function of time t. For real time AFM imaging, the function $s(t)$ has to be calculated offline *a priori*. Specifically, the function $t(s)$ can be approximated by curve-fitting and then the inverse of the function $t(s)$ is the function of s with respect to time t.

3. Weighted prediction algorithm

3.1. A recursive least square prediction method

When scanning simple object samples, nearby contours are similar to each other and it can be assumed that there is some projection (translation, scaling and rotation) which relates these close contours. Therefore, a currently partially scanned contour can be estimated using information from previously scanned contours. Here, we propose a least squares approximation of the currently scanned contour depending on previously scanned data.

In practice, the suggestion is to scan the target sample starting with contours at a lower height, advancing to the top point of the specimen: this is sensible as the uncertainty at the very top contour is the most significant due to noise. The current scanning contour is always higher and in diameter/area smaller than previously scanned contours. Thus, the currently scanned contour may be called the inner contour, Y, and the previously scanned contour is the outer contour, X.

Suppose the measured points from the previous scan are $X = [X_1, X_2, \ldots, X_k, ..X_N]$, where each point $X_k = \begin{bmatrix} X_{kx} & X_{ky} \end{bmatrix}^T$ is represented in Cartesian coordinates. Due to the small distances between the points in X, the centre (the mean) of X_k, $C = \left[\left(\sum_k X_{kx} / N \right) \ \left(\sum_k X_{ky} / N \right) \right]^T$, can be used as a reference point for a map between a point on the outer contour X to a point on the inner contour Y; N denotes the number of points in X. The normalized vector from one point X_k on the outer contour to the centre C is defined as $V_k = X_k - C / \| X_k - C \|$. To find a relationship between the inner and outer contours, suppose one point Y_k on the inner contour is obtained from the point X_k on the outer contour along the vector V_k. In this way, Y_k, can be mapped from X_k by a transformation given by

$$Y_k = \mathcal{A}X_k + \mathcal{B}, \ \text{or} \ Y_k = [\mathcal{A}|\mathcal{B}] \begin{bmatrix} X_k \\ 1 \end{bmatrix}, \tag{6}$$

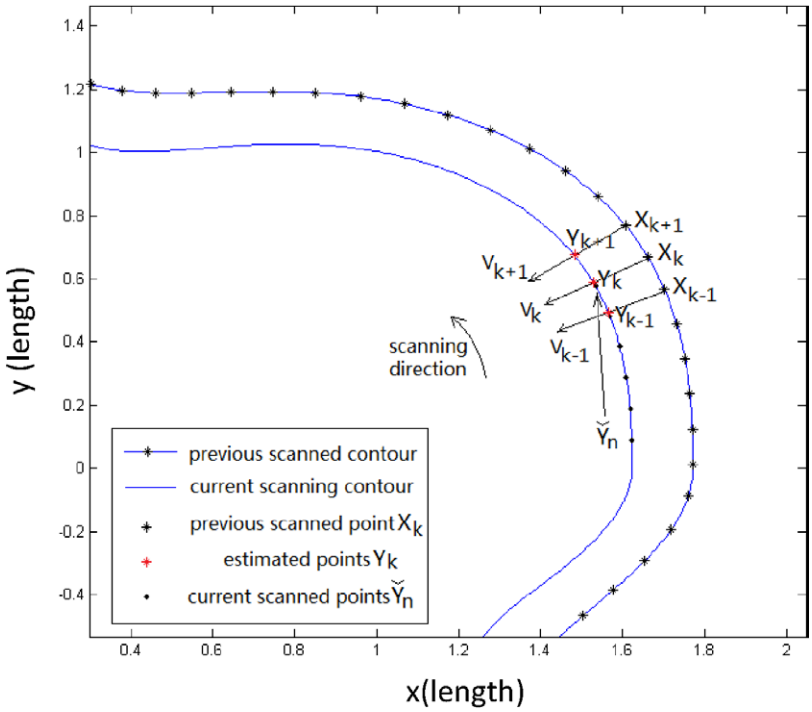

Figure 3. Demonstration of a prediction using the RLS filter.

where $\mathcal{A}$ is a two-by-two matrix and $\mathcal{B}$ is a vector with two elements. Here matrix $\mathcal{A}$ can represent a rotation or a contraction towards the centre point C, while $\mathcal{B}$ represents a simple translation. As a result, the currently scanned inner contour can be estimated from the previous outer contour and an appropriate transformation map.

However, an accurate approximation of the map $[\mathcal{A}|\mathcal{B}]$ is not available *a priori*. Here, a recursive least squares (RLS) approach is proposed to estimate the map, which allows an incremental improvement. Thus, it is necessary for the contour Y to obtain some initial measurement values $\breve{Y}_1$, $\breve{Y}_2$,…, within the current inner contour scan without the use of the map $[\mathcal{A}|\mathcal{B}]$. This creates a growing sequence of discrete points $\breve{Y}$ measured on the inner contour: $\breve{Y} = [\breve{Y}_1, \breve{Y}_2, \ldots, \breve{Y}_n]$, where $\breve{Y}_i$ represents the measured points on the (partially) measured inner contour and n is the number of obtained points on the currently scanned contour (figure 3). In the current inner contour scan, Y_k represents the closest crossing point of V_k on the contour line created by $\breve{Y}$. The point X_k is the starting point of the vector V_k to provide Y_k. Thus, when the tip measures a new point on the inner contour, the points $Y_k = \begin{bmatrix} Y_{kx} & Y_{ky} \end{bmatrix}^T$ on the currently scanned contour and $X_k = \begin{bmatrix} X_{kx} & X_{ky} \end{bmatrix}^T$ on the outer contour are obtained. The transfer map can be rewritten as

$$Y_{kx} = {w_x}^{\mathrm{T}} \begin{bmatrix} X_k \\ 1 \end{bmatrix}, Y_{ky} = {w_y}^{\mathrm{T}} \begin{bmatrix} X_k \\ 1 \end{bmatrix}, \tag{7}$$

where w_x and w_y are the two vectors defining the map $[\mathcal{A}|\mathcal{B}]$, where $Y_{k,x}$ and $Y_{k,y}$ denote the x and y values of Y_k. Therefore the RLS updating equations [14] at step k are given by

$$N_{k,m} = H_{k,m} \begin{bmatrix} X_k \\ 1 \end{bmatrix}, \tag{8a}$$

$$K_{k,m} = \frac{N_{k,m}}{\lambda + \begin{bmatrix} X_k \\ 1 \end{bmatrix}^T N_{k,m}}, \tag{8b}$$

$$\theta_{k,m} = Y_{k,m} - {w_{k,m}}^T \begin{bmatrix} X_k \\ 1 \end{bmatrix}, \tag{8c}$$

$$w_{k+1,m} = w_{k,m} + K_{k,m}\theta_{k,m}, \tag{8d}$$

$$H_{k+1,m} = \lambda^{-1}H_{k,m} - \lambda^{-1}K_{k,m}\begin{bmatrix} X_k \\ 1 \end{bmatrix}^T H_{k,m}, \tag{8e}$$

where $m = x$ or y indicates the index in terms of the relevant Cartesian coordinate elements. The scalar λ is a constant, positive parameter, which is set to be equal to or smaller than 1. Often it is set slightly less than 1 to allow for exponential weighting of the error $\theta_{k,m}$ and subsequent forgetting of earlier data X_k. For initialization, all elements in w_k equal 0 and H_k is an identity matrix. Thus, with the RLS filter, the map is estimated online for the current contour scan by

$$[\mathcal{A} \mid \mathcal{B}] = [w_x \quad w_y]^T. \tag{9}$$

In the RLS filtering process, the most recently updated information influences the results more than old data [14], depending on the choice of λ. Therefore, the estimated map will adapt with respect to the changing inner contour. The next section will suggest a suitably weighted combination of this RLS-based algorithm with the contour prediction algorithm of Andersson from section 2 (see [10]).

3.2. Combined prediction via adaptive weighting

Andersson's prediction algorithm in section 2 provides a contour estimate from three new scanned points on the current contour (2)–(3). Here we name this as the current-prediction, because such a prediction of the curve states is only based on information from the currently scanned contour. The estimated heading direction and curvature are introduced as θ_{cur} and κ_{cur}. On the other hand, the RLS-prediction, described in section 3.1, predicts the next points based on both the currently scanned inner and the recently scanned outer contours. With these estimated points, the curve states representing heading angle θ_{RLS} and curvature κ_{RLS} can be calculated.

In this work, we propose a prediction algorithm, which combines the current-prediction and the RLS-prediction to achieve increased accuracy. In practice, two estimated contour states, which are given by $\begin{bmatrix}\theta_{\text{cur}} & \kappa_{\text{cur}}\end{bmatrix}^T$ and $\begin{bmatrix}\theta_{\text{RLS}} & \kappa_{\text{RLS}}\end{bmatrix}^T$, are weighted to provide the prediction of the contour model for driving the tip. A simple weighting law is

$$\begin{bmatrix}\theta_{\text{e}}\\ \kappa_{\text{e}}\end{bmatrix} = W_{\text{cur}}\begin{bmatrix}\theta_{\text{cur}}\\ \kappa_{\text{cur}}\end{bmatrix} + W_{\text{RLS}}\begin{bmatrix}\theta_{\text{RLS}}\\ \kappa_{\text{RLS}}\end{bmatrix},\ W_{\text{RLS}} + W_{\text{cur}} = 1. \tag{10}$$

The errors from the two predictions are introduced as the variables to be used for evaluating the weights. Using the estimation method introduced in [3], the estimated position of a point on the curve can be calculated from the update law using the curve states via

$$P_k = \overline{P}_{k-1} + \begin{cases} \dfrac{M(\kappa_k \mathrm{d}s)}{\kappa_k}\begin{pmatrix} q_{1k}\\ q_{2k}\end{pmatrix}, & \kappa_k \neq 0\\ q_{1k}\mathrm{d}s, & \kappa_k = 0\end{cases}, \tag{11}$$

where $M(\alpha) = \begin{pmatrix}\sin\alpha & 0 & 1-\cos\alpha & 0\\ 0 & \sin\alpha & 0 & 1-\cos\alpha\end{pmatrix}$.

Here P_k represents the predicted point at arclength s when the $(k-1)$th point $\overline{P}_{k-1}$ is measured. Here, κ_k, q_{1k}, and q_{2k} represent the estimates of the kth curve states (see (2) and (3) in section 2). Thus, the current-prediction and the RLS-prediction give two estimates of the position of the point as $P_{\text{cur},k}$ and $P_{\text{RLS},k}$ at arclength s. With a new measured point $\overline{P}_k$ on the contour, the Euclidean distances from $\overline{P}_k$ to $P_{\text{cur},k}$ and $P_{\text{RLS},k}$ are introduced as the errors in the two prediction methods. Here the Euclidean distances are used as the evaluation variables for the following reasons: (a) low computational complexity, (b) ease of evaluation compared to the errors of estimated contour states, (c) simplicity of use as a 1D value. Thus, the errors in the current-prediction and the RLS-prediction are defined by

$$e_{\text{cur}.k} = \|P_{\text{cur}.k} - \overline{P}_k\|_2,\ e_{\text{RLS}.k} = \|P_{\text{RLS}.k} - \overline{P}_k\|_2. \tag{12}$$

To avoid the effect of considerable noise in the errors, the weights from the two predictions are obtained by (statistically) averaging the errors of both predictions over time. Additionally, the current estimation performance is more important than old data for accurate contour tracking. Therefore an update algorithm, using a filter approach, was utilized to assess the errors of the two predictions:

$$\widehat{W}_{\text{cur}.k} = e_{\text{cur}.k} + \alpha\widehat{W}_{\text{cur}.k-1}, \tag{13a}$$

$$\widehat{W}_{\text{RLS}.k} = e_{\text{RLS}.k} + \alpha\widehat{W}_{\text{RLS}.k-1}, \tag{13b}$$

where $\widehat{W}_{\text{cur}}$ and $\widehat{W}_{\text{RLS}}$ are the filter variables for the current-data-prediction and the RLS-prediction, and α is a forgetting factor to consider the history of the errors. Then the weights W_{cur} and W_{RLS} are obtained by normalizing the updates $\widehat{W}_{\text{cur}}$ and $\widehat{W}_{\text{RLS}}$ as

$$W_{\text{cur}} = \frac{\widehat{W}_{\text{RLS}}}{\widehat{W}_{\text{RLS}} + \widehat{W}_{\text{cur}}},\ W_{\text{RLS}} = \frac{\widehat{W}_{\text{cur}}}{\widehat{W}_{\text{RLS}} + \widehat{W}_{\text{cur}}}. \tag{14}$$

At the beginning of the scanning of one contour, W_{cur} is initialized as 0 and W_{RLS} is 1, while $\widehat{W}_{\text{cur}}$ and $\widehat{W}_{\text{RLS}}$ are set to 0 since there is no efficient estimation from the current-prediction methods until three points on the contour have been obtained. They will be calculated after the first three points on the contour have been measured. In addition, the forgetting parameter α is a positive constant smaller than 1. Note that when α equals 1, all historical errors can influence the weighted prediction.

As more points are measured, the overall performance of the weighted prediction improves, and the curve is estimated with an increasing accuracy. Furthermore, there is no need for driving the tip with a very large searching region to ensure an efficient error-free scan, and the tip can be kept in a very small neighbourhood of the sample contours. Therefore, the parameter A, which determines the tip searching range, can be adjusted to the prediction accuracy. One possible choice is

$$A = \begin{cases} A_{\max} & \text{if } \max\left[\widehat{W}_{\text{cur}}, \widehat{W}_{\text{RLS}}\right] \geq A_{\max}\\ A_{\min} & \text{if } \max\left[\widehat{W}_{\text{cur}}, \widehat{W}_{\text{RLS}}\right] \leq A_{\min}\\ \max\left[\widehat{W}_{\text{cur}}, \widehat{W}_{\text{RLS}}\right], & \text{elsewhere}\end{cases}. \tag{15}$$

Here, the parameter $A_{\min}$ is set as the smallest amplitude of the tip trajectory, and parameter $A_{\max}$ is set as the maximal scanning amplitude. As a consequence, the tip can move away from or closer to the contour boundary for measuring the next point on the curve. In this way, the impact of (considerable) noise in the error can be eliminated to some extent.

A guarantee that the algorithm can scan a set of closed contours is easily obtained using arguments from Chang and Andersson [10] and general ideas on RLS-algorithms [14].

Remark 1: The adaptive non-raster algorithm is guaranteed to provide a scan of a finite set of smooth closed contours (starting at a bottom contour) provided each inner contour can be described via a linear map (6) resulting from an outer, lower contour, and the parameters $A_{\min}$ (15) and ω satisfy: [10]

$$A_{\min} > \frac{1}{\kappa_{\max}} - \sqrt{\frac{1}{\kappa_{\max}^2} - \frac{9\pi^2}{4\omega^2}}, \tag{16}$$

where $\kappa_{\max}$ is the largest contour curvature. In addition, it is required that the forgetting factor λ in the RLS algorithm satisfies $0 < \lambda < 1$ and that in the error update algorithm (13), the parameter α satisfies $0 < \alpha < 1$.

An argument to show validity of the statement above is provided in the appendix.

Remark 2: In a noise free environment, when all the assumptions of Remark 1 are satisfied, the two predictions using the current and previous contour information should be identical. The advantage of this combined algorithm is when it is used in a practical environment where noise and specimen inaccuracies are observed.

Remark 3: The proposed non-raster algorithm is capable of scanning a specimen with a single maximum (or a single minimum). It is designed to speed up the scanning of a specimen and to permit repeated scans of the same specimen area to investigate dynamic changes. In the case of several extrema in the specimen area of interest, it would be sensible to introduce at the beginning of a scan, information about the local minima and maxima within the area of interest, allowing the subsequent local use of the non-raster scanning approach. It is expected that such local extrema do not significantly change position despite the dynamic changes of the specimen. Initial information about local extrema can be achieved via a global raster scan of the area of interest. An alternative is to use a local search algorithm for some extrema to provide reasonable information before the start of the non-raster scan, e.g. [26] or [6]. This could also be complemented by area partitioning methods known from reconnaissance techniques [5].

4. Default *Z*-positioning scheme and adaptive gradient based *Z*-positioning improved scanning

For successive contour scans, a constant height step for the cantilever tip is simple and fairly effective, as demonstrated later. It is best to start from the bottom to allow the first contour to be collected and to use the combined trajectory prediction algorithm. One issue is that the tip may fail to properly scan the top of the sample, because the upper-most contours are usually of very small scale. To scan the sample profile, the decision about the z-axis step size, i.e. the vertical changes between contours, influences the imaging quality. However, if the sample is like a cell or a bacterium, the surface topography might be very steep at the bottom, while a flattened profile is observed at the top. Hence, there is no need to measure similar contours at the bottom for topography imaging and it is better to measure the contours at the heights where the contours change most. This is in particular where the slope of the specimen is low (often at the top of the specimen). Thus, an adaptive z-positioning method is introduced to avoid small steps for consistently steep parts of the specimen, where there is little change in contour.

To achieve adaptive z-positioning, the average topography gradient across a contour in the vertical direction, and the change in gradient, needs to be predicted. Knowing the current vertical step size, the average distance in the x–y plane from the current scanning contour and the next contour is calculated initially. Hence, at the ith step, during one contour scan, the new measured point on the contour is $\overline{Y_i} = [\overline{Y_{ix}} \;\; \overline{Y_{iy}}]^T$ and the matching point on the previous contour can be found as $\overline{X_i} = [\overline{X_{ix}} \;\; \overline{X_{iy}}]^T$. The ith distance can be calculated as $d_{k,i} = \| Y_i - X_i \|_2$. The additional index k indicates here that the data $\overline{Y_i}$ is taken from the currently scanned kth contour. At the end of the kth contour scan, the distance from the kth scanned contour to the $(k-1)$th contour is on average $\overline{d}_k = \sum_{i=1}^{N} d_{k,i} / N$, where N is the number of measured points during the kth contour scan. The displacement of z-axis (height) from the $(k-1)$th contour to the kth contour is Δz_k. Thus, the gradient of the sample profile changes is defined as

$$g_k = \Delta z_k / \overline{d}_k. \tag{17}$$

At the kth contour scan, the ratio of the changing gradients is estimated as

$$r_k = (g_k - g_{k-1}) / g_{k-1}. \tag{18}$$

Then, the ratio is used for estimating the step height z_{k+1} to obtain the next z-axis value (scanning height) for the $k+1$th contour given an expected distance E_d in the x–y plane:

$$g_{k+1} = g_k + r_k g_k, z_{k+1} = \begin{cases} z_{\min}, E_d g_{k+1} < z_{\min} \\ z_{\max}, E_d g_{k+1} > z_{\max} \\ E_d g_{k+1}, \text{elsewhere} \end{cases}. \tag{19}$$

Here g_{k+1} is the estimated gradient of the $k+1$th contour with respect to the kth contour. To eliminate the effects of noise, the displacement step of the z-position is restricted to an interval: i.e. $z_k \in [z_{\min}, z_{\max}]$, where $z_{\min}$ and $z_{\max}$ are the minimal and maximal values of z-displacements. Hence, the adaptive z-positioning scheme provides a step function z_{k+1} to ignore similar contour scans, which may lead to greater scanning efficiency.

5. Delaunay triangular interpolation for imaging

To obtain an image from the scanning results, it is necessary to introduce an image interpolation algorithm to turn non-raster scanned data into (comparable) rastered-images. Recent image interpolation methods assume for the Kriging interpolation [15] that the specimen is string-like. In contrast, a Delaunay triangular interpolation [15] algorithm is used here to achieve fast, online-imaging from non-raster scanned data. The Delaunay triangulation sorts the scanned image into a unique set of triples of points [18], which is achieved by maximizing the smallest angle of every triangle formed by a triple of points. For instance, consider a triple constructed from three points: O, P, and Q. At these three positions, the measured profile height values are V_O, V_P, and V_Q. The interpolated height value V_I at any point I is approximated as

$$V_I = \frac{S_{IPQ} V_A + S_{OIQ} V_P + S_{OPI} V_Q}{S_{OPQ}}, \tag{20}$$

where S denotes the area of the triangle constructed by the points, *IPQ, OIQ, OPI* or *OPQ*. Thus, the height data can be computed at each pixel point I. It is evident that this interpolation algorithm is fast due to its local character.

In contrast, there are many global algorithms [8, 23, 24], which can compute, within several iterations from existing incomplete image data, a global image model, allowing for

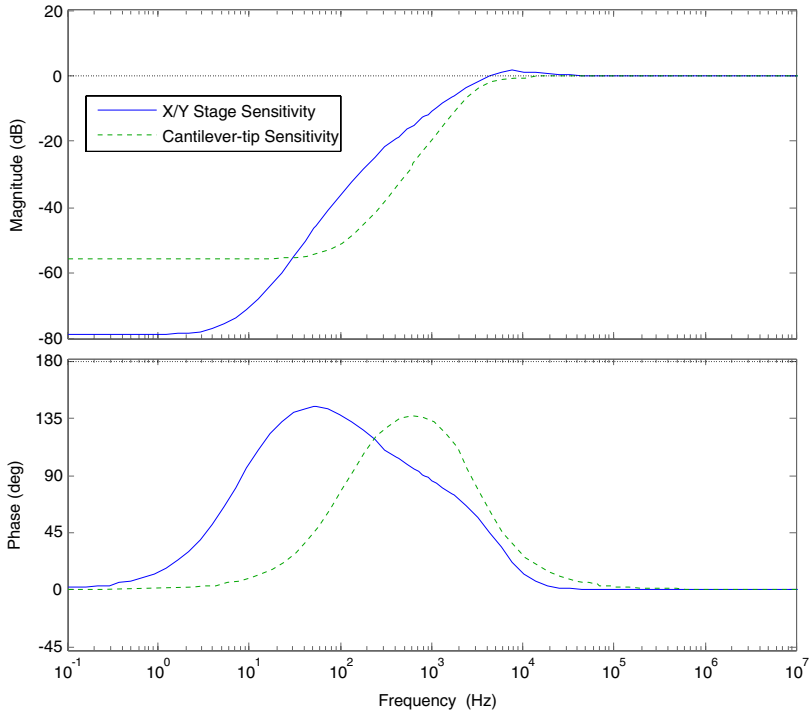

Figure 4. Closed loop sensitivity response of *x*-, *y*- and *z*-control.

highly effective interpolation. These algorithms are very powerful and they can predict topology curvature and other topology derivatives at a high order. They can potentially produce excellent results, but are not suited yet for real-time implementation. Hence, the Delaunay approach is preferred here, since an interpolated image can be obtained from the Delaunay triangulation with one single computational iteration: i.e. it can be (in principle) easily implemented online, resulting in a fast stream of continuous rastered images.

6. Simulation results

6.1. Setup for practically relevant evaluation

Several tests were conducted in order to investigate the performance of the non-raster scanning method. To create a realistic simulation, dynamic models of a piezo-actuated *x*–*y* horizontal stage and the vertical *z*-motion for the piezo-actuated tip-cantilever control are included. The *x*–*y* stage dynamics are assumed to have a resonance frequency at 870.6 Hz with a damping ratio of 0.1282 [16]. The *Q*-factor of the *z*-cantilever actuation dynamics is 210 with a resonance frequency at 7.45 kHz [17]. Using a mixed sensitivity *H*-infinity control design [25], the controller bandwidth for the *x*–*y* actuator is 1.59 kHz and the bandwidth for the tip-cantilever is 7.33 kHz for a fast robust response (see figure 4).

The specimen in our simulation is chosen as an upper half ellipsoid, similar to a real cell 3D image from an AFM given in [27]. However, here we scale the specimen to be smaller with a typical height value of 250 nm to represent bacteria in air [29]. The ellipsoid radii of the target specimen in the simulations are 300 nm along the *x*-axis, and 400 nm along the *y*-axis. Thus, for raster scanning, the substrate is best scanned for a frame of 800 nm along the *x*-axis and of 1000 nm along the *y*-axis. The imaging resolution is set to achieve a pixel size of $(10\,\text{nm})^2$ per pixel. Thus, the Delaunay triangular interpolation algorithm will be used to approximate images with pixels of that size for the suggested non-raster scanning algorithms. Following the dynamics of the horizontal control, the scanning speed is set to $10\,\text{mm}\,\text{s}^{-1}$ for accurate control performance.

6.2. Results and discussions

Scanning approaches in AFM are often evaluated by scanning time and imaging quality. In particular, imaging quality is evaluated here in the form of an error per-pixel:

$$e_{\text{PP}} = \frac{\sum_{i,j} \sqrt{(V_{i,j} - O_{i,j})^2}}{N}, \tag{21}$$

where $V_{i,j}$ indicates the imaged height at the (i, j) pixel and $O_{i,j}$ stands for the ideal height at position (i, j) derived from the original 80-by-100 pixel data. The total number of pixels is $N = 8000$.

The raster scan takes 8.0118 s and the error per pixel is $e_{\text{PP}} = 2.6626$ nm (see figure 5). The largest imaging errors can be found at the edge of the specimen due to the bandwidth limits of the *z*-control loop.

For the non-raster scanning method, the scan starts at the bottom and scans at a height of 5 nm. The chosen sample has a curvature radius between 225 nm for contours close to the sample top at a height of 248.4 nm, and 534 nm for the bottom contour at a height of 5 nm. Considering the relationship between ω, A and the curvature of target contours in [10], the scanning parameters are set as $\omega = 0.3$, $A_{\min} = 3$ nm, $A_{\text{initial}} = A_{\max} = 8$ nm to be able to scan curves with a minimal curvature

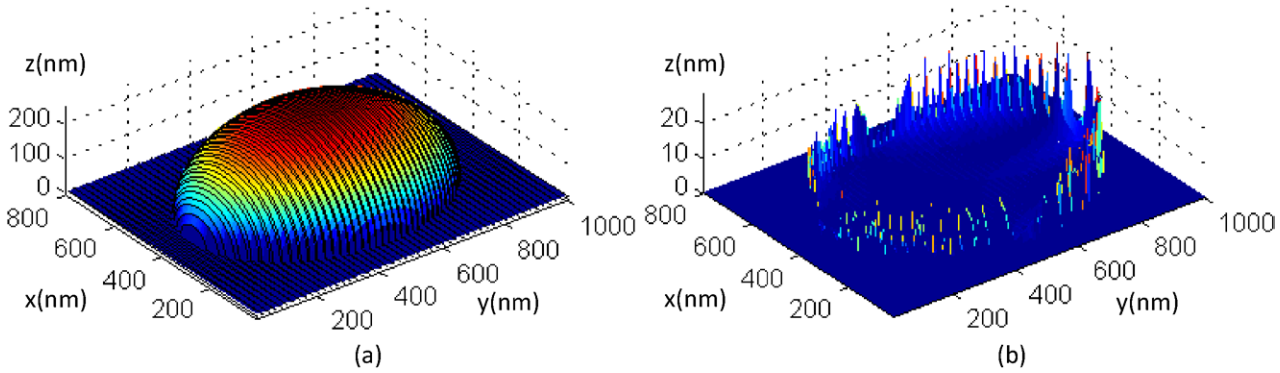

Figure 5. 3D image (color) using raster scan; tip trajectory (black) in (*a*); the absolute errors for each pixel (*b*).

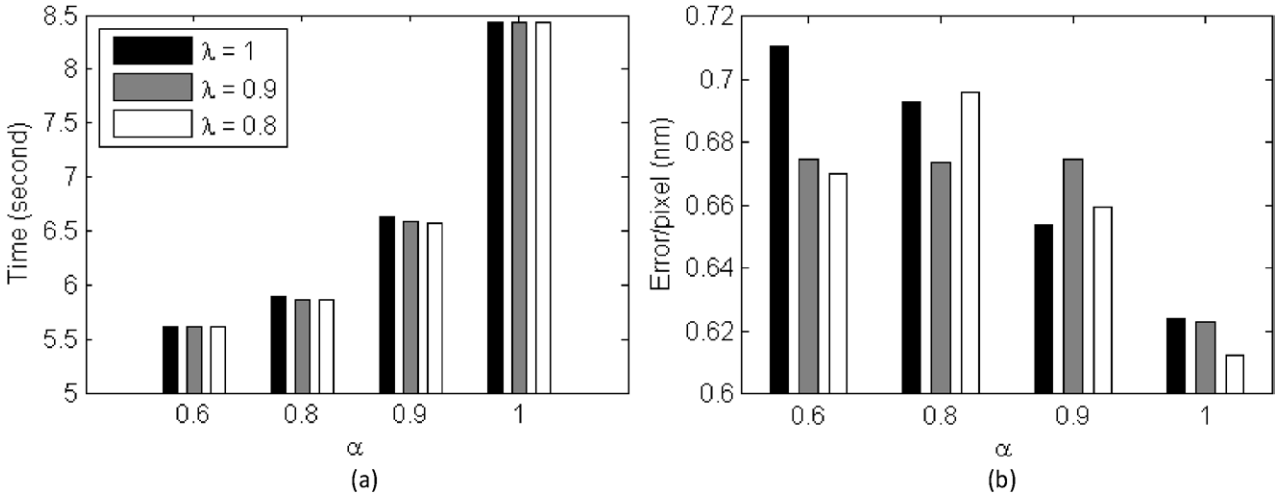

Figure 6. Scanning time (*a*) and e_{PP} (*b*) as a function of parameters λ and α for non-raster scanning with constant z-step.

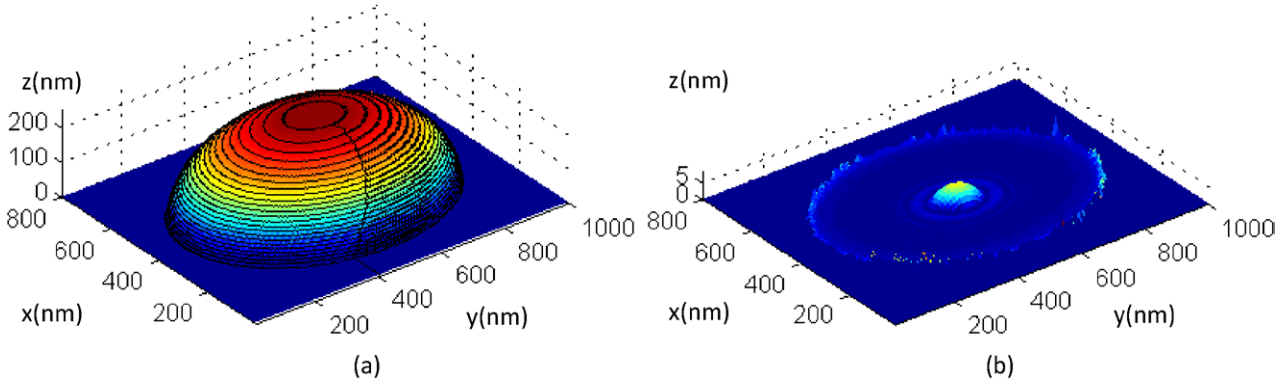

Figure 7. Non-raster scan with constant z-step; tip trajectory (black) in (*a*); the absolute errors for each pixel (*b*).

radius as small as 43 nm (as in Remark 1 and equation (16)). This robustly permits the scanning trajectory to achieve successful scans until a height of 248.4 nm.

For constant height step z-positioning of the non-raster scanning approach, the step size is set as 10 nm. The scanning time and e_{PP} with respect to α (13) and λ (8) are demonstrated in figure 6.

From figure 6, it is clear that the scanning time is higher with higher α. The scanning time drops significantly when α is smaller than 0.9. However, α has little influence on the error–per-pixel evaluation when α is less than 1. Thus, α is suggested to be around 0.8 to permit a fast scan with a small e_{PP}. In general, a range between $\alpha = 0.9$ to $\alpha = 0.6$ appears to be the most suitable. The forgetting factor λ affects the scanning time and the error–per-pixel measure e_{PP} to a small extent; to ensure a stable predictable imaging quality, λ is suggested as 0.9. In the proposed method, the setup is suggested as $\alpha \approx 0.8$ and $\lambda = 0.9$. For $\alpha = 0.8$ and $\lambda = 0.9$, the results for the constant-step z-positioning non-raster scan are given in figure 7.

With the same parameter (ω, A_{min}, $A_{initial}$, and A_{max}) setup, simulations have been conducted for the non-raster scanning method employing the adaptive z-positioning scheme. In practice, the expected distance between two nearby contour scans relates to the resolution requirements, i.e. if the distance is

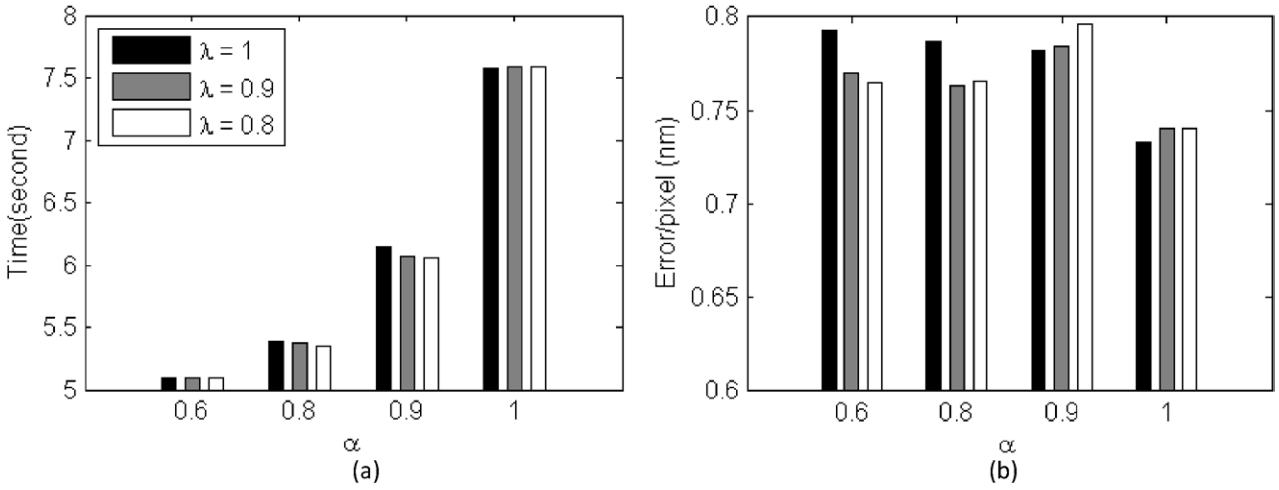

Figure 8. Scanning time (*a*) and e_{PP} (*b*) as a function of parameters λ and α for non-raster scanning with adaptive z-step.

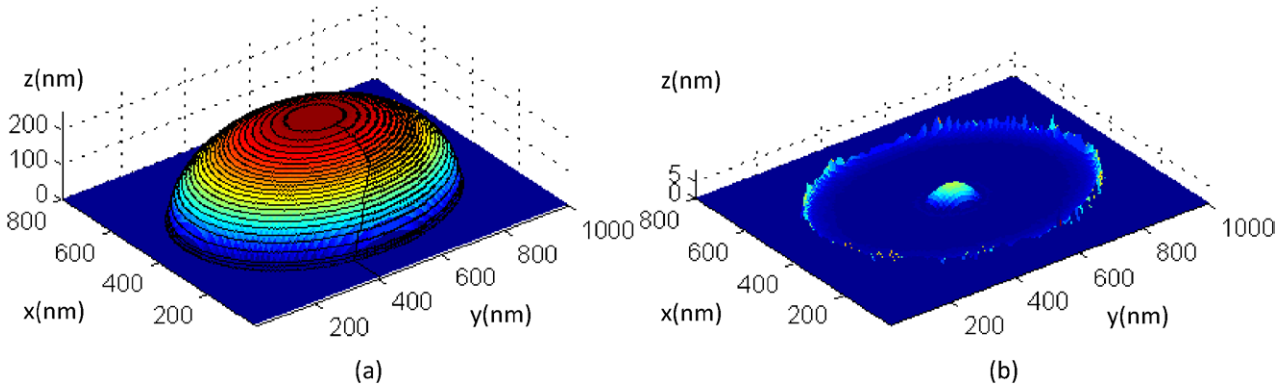

Figure 9. Non-raster scan with adaptive z-step; tip trajectory (black) in (*a*); the absolute errors for each pixel (*b*).

set as 10 nm, the final image will have pixel sizes of $(10\,\text{nm})^2$ per pixel. The limits for the z-positioning step are set as z_{min} = 6 nm and z_{max} = 26 nm. This implies scanning contours of at least 9 and less than 50 for this sample. The ideal number of scanned contours should be around 30 in our simulation due to the sample size and the required resolution. The adaptive z-positioning scheme works well in all simulated circumstances. The scanning performance is illustrated in figure 8.

Similar to the results using the constant z-positioning step, the parameter choice of $\alpha \approx 0.8$ and $\lambda = 0.9$ provides a robust and most promising parameter choice considering both scanning speed and imaging quality. The 3D image is shown in figure 9. It is evident that the adaptive z-positioning scheme introduces robustness to noise. This has also been confirmed in simulation following the addition of Gaussian sensor noise with a standard deviation of 0.2 nm, which is a practical choice considering the accuracy of the available sensors in force microscopy. Interestingly, there is only a minor increase (less than 2%) in the scanning time and the scanning error so that any extra representation of the results is avoided here.

From these results it is evident that the non-raster scanning approaches provide at least a 26.7% faster scan and a much more accurate imaging quality than a classical raster scan, as the error per pixel measure improves from 2.6626 nm to less than 0.8 nm. Clearly, this is avoided by the less stringent need for a high controller bandwidth in the z-direction.

The advantage of the adaptive z-step approach is not necessarily a significantly improved scanning quality, but a higher flexibility and a greater robustness of the set-up of the z-height steps. It should also be noted that for the two non-raster scanning schemes, the tip will reach neither the very top of the target specimen nor the very bottom contours. The errors in the proposed non-raster scanning method mainly come from the top and the bottom but this can be improved by the adaptive z-stepping scheme. Another positive effect of the adaptive z-stepping scheme is the greater density of scanning contours at the usually less steep top of the specimen (see figure 7(*a*) for the constant z-step scheme versus figure 9(*a*)). The 'jump' effects caused by the vertical dynamics are avoided and the possible imaging error can be reduced to some extent.

7. Conclusions

In this paper, we have proposed a novel non-raster scanning method which achieves high accuracy and high speed scanning for simple object samples compared with raster scans. A new scanning trajectory is introduced to avoid damage to the specimen, as the trajectory will not cross into the specimen. Moreover, the trajectory permits a dynamically adjusted amplitude, while a prediction algorithm fuses information from the currently scanned and the most

recently scanned contours. The scanning trajectory is adaptive to the sample surface profile. The use of the Delaunay Triangular interpolation provides an efficient way to turn raw data into images.

Practically relevant simulations have introduced realistic dynamics of the actuation and position control mechanism in the x–y and z-height direction. The simulation results show overall that this provides faster and much more accurate non-raster scanning than typical raster scanning approaches under the same conditions.

Acknowledgments

We would like to acknowledge the support of the Engineering and Physical Sciences Research Council (EPSRC) (grant nos. EP/I034882/1 & EP/I034831/1).

Appendix. Remark 1—stability of the non-raster scanning algorithm

The argument for stability is split into three steps. In the first step, it is argued that the new trajectory r_t (4) follows the basic principles of Chang and Andersson [10], i.e. the novel trajectory guarantees specimen scanning even for an adapted amplitude. In the second step, it will be argued that the RLS-algorithm (7)–(8) is stable. The final, third step will demonstrate that the overall combined algorithm is stable and converging:

Step 1: Consider the new trajectory r_t from (4) and the trajectory designed by Chang and Andersson [10 equation (2)],

$$r_A(s) = r_d(s) + A\sin(\omega(s))\, q_2(s).$$

The trajectory of Chang and Andersson is identical to the new trajectory r_t (4)

$$|r_A(s)| = |r_t(s)|, \text{for} \frac{\pi}{2\omega} \leq s - s_i,$$

where s_i is a crossing point of the trajectory $r_A(s)$ or $r_t(s)$ on the contour. Once the arc variable satisfies $\pi/2\omega \leq s - s_i$, the trajectory approaches the contour. Chang and Andersson [10] provide, for that reason, a minimal (possibly conservative) value (16) for the amplitude A. It is evident that an increase of this amplitude improves the chance of the trajectory $r_t(s)$ intersecting the specimen contour. Thus, considering Chang and Andersson [10], the suggested trajectory resulting from (2)–(4) is guaranteed to successfully scan a closed contour for a given worst case contour value κ_{max} and amplitude constraint (16).

Step 2: The linear map (7) allowing for rotation, translation and contraction, has 2 × 3 parameters to be estimated, where three parameters are used for the map of Y_{kx} and another three for the map of Y_{ky}. The RLS-algorithm in (7)–(8) is only used once the second contour is scanned and at least three distinct points $Y_1, Y_2, Y_3, \ldots, Y_k$ are measured, as a map from points $X_1, X_2, X_3, \ldots, X_k$ on the previous contour. In this case, the RLS-algorithm converges after the first three distinct points Y_1, Y_2, Y_3 are measured.

Step 3: In a noise free, ideal environment, the two predictions of the curvature and gradient using the current and previous contour should be identical so that $\begin{bmatrix}\theta_e\\ \kappa_e\end{bmatrix} \approx \begin{bmatrix}\theta_{cur}\\ \kappa_{cur}\end{bmatrix} \approx \begin{bmatrix}\theta_{RLS}\\ \kappa_{RLS}\end{bmatrix}$. This leads to a successful scan of the set of contours for given largest curvature κ_{max}.

References

[1] Abramovitch D Y, Andersson S B and Pao L Y 2007 A tutorial on the mechanisms, dynamics, and control of atomic force microscopy *American Control Conf. (New York, 9–13 July)* pp 3488–502

[2] Anczykowski B, Cleveland J P, Krüger D, Elings V and Fuchs H 1998 Analysis of the interaction mechanisms in dynamic mode SFM by means of experimental data and computer simulation *Appl. Phys.* A **66** 885–9

[3] Andersson S B 2007 Curve tracking for rapid imaging in AFM *IEEE Trans. Nanobiosci.* **6** 354–61

[4] Ando T 2012 High-speed atomic force microscopy coming of age *Nanotechnology* **23** 062001

[5] Baillieul J and Baronov D 2010 Information acquisition in the exploration of random fields *Three Decades of Progress in Control Sciences* (Berlin: Springer) pp 1–17

[6] Baronov D and Baillieul J 2011 A motion description language for robotic reconnaissance of unknown fields *Eur. J. Control* **17** 512–25

[7] Binnig G, Quate C F and Gerber C 1986 Atomic force microscope *Phys. Rev. Lett.* **56** 930–3

[8] Burger M, He L and Schönlieb C-B2009 Cahn–Hilliard inpainting and a generalization for grayvalue images *SIAM J. Imaging Sci.* **2** 1129–67

[9] Brown B P, Picco L, Miles M J and Faul C F J2013 Opportunities in high-speed atomic force microscopy *Small* **9** 3201–11

[10] Chang P I and Andersson S B 2009 Theoretical bounds on a non-raster scan method for tracking string-like samples *American Control Conf. (St. Louis, MO, 10–12 June)* pp 2266–71

[11] Chang P I , Huang P, Maeng J and Andersson S B 2011 Local raster scanning for high-speed imaging of biopolymers in atomic force microscopy *Rev. Sci. Instrum.* **82** 063603

[12] Chen Y and Huang W 2004 Numerical simulation of the geometrical factors affecting surface roughness measurements by AFM *Meas. Sci. Technol.* **15** 2005–10

[13] Chen Y and Huang W 2007 Some issues on atomic force microscopy based surface characterization *Optoelectron. Lett.* **3** 129–32

[14] Haykin S O 2001 *Adaptive Filter Theory* 4th edn (Upper Saddle River: Prentice-Hall) chapter 9

[15] Huang P and Andersson S B 2011 Generating images from non-raster data in AFM *2011 American Control Conf. (San Francisco, CA, 29 June–1 July)* pp 2246–51

[16] Huang P and Andersson S B 2012 Fast scanning in AFM using non-raster sampling and time-optimal trajectories *51st IEEE Conf. on Decision and Control (Hawaii, 10–13 December)* pp 5073–8

[17] Huang P and Andersson S B 2013 *Experimental Verification of High Speed AFM Through Local Raster Scanning (Washington, DC, 17–19 June)* pp 6063–8

[18] Lee D T and Schachter B J 1980 Two algorithms for constructing a Delaunay triangulation *Int. J. Comput. Inf. Sci.* **9** 219–42

[19] Marinello F, Savio E, Bariani P and Carmignato S 2009 Coordinate metrology using scanning probe microscopes *Meas. Sci. Technol.* **20** 084002

[20] Miles M, Antognozzi M, Haschke H, Hobbs J, Humphris A and McMaster T 2003 Tour de force microscopy *Mater. Today* **6** 30–7
[21] Müller D J and Dufrêne Y F 2011 Atomic force microscopy: a nanoscopic window on the cell surface *Trends Cell Biol.* **21** 461–9
[22] Seah M P 2014 Measurement of the roughness of nano-scale surfaces, both unannealed and with limited anneal, by atomic force microscopy *Meas. Sci. Technol.* **25** 105001
[23] Schönlieb C-B and Bertozzi A 2011 Unconditionally stable schemes for higher order inpainting *Commun. Math. Sci.* **9** 413–57
[24] Schönlieb C-B 2011 Higher-order total variation inpainting (www.mathworks.com/matlabcentral/fileexchange/34356-higher-order-total-variation-inpainting/content/HigherOrderTVinpainting.zip), MATLAB Central File Exchange, Updated 7 August 2012
[25] Skogestad S and Postlethwaite I 2007 *Multivariable Feedback Control: Analysis and Design* 2nd edn (New York: Wiley)
[26] Snyman J A2005 *Practical Mathematical Optimization: An Introduction to Basic Optimization Theory and Classical and New Gradient-Based Algorithms* (Berlin: Springer)
[27] Tamayo J, Humphris A D L, Owen R J and Miles M J 2001 High-Q dynamic force microscopy in liquid and its application to living cells *Biophys. J.* **81** 526–37
[28] Uchihashi T, Kodera N and Ando T 2012 Guide to video recording of structure dynamics and dynamic processes of proteins by high-speed atomic force microscopy *Nat. Protocols* **7** 1193–206
[29] Velegol S B, Pardi S, Li X, Velegol D and Logan B E 2003 AFM imaging artifacts due to bacterial cell height and AFM tip geometry *Langmuir* **19** 851–7
[30] Wang C and Itoh H 2013 A simulation study for evaluating and improving the accuracy of surface roughness measured by atomic force microscopy *Meas. Sci. Technol.* **24** 035401
[31] Yacoot A and Koenders L 2011 Recent developments in dimensional nanometrology using AFMs *Meas. Sci. Technol.* **22** 122001
[32] Yagasaki K 2010 New control methodology of microcantilevers in atomic force microscopy *Phys. Lett.* A **375** 23–8
[33] Yong Y K, Moheimani S O O and Petersen I R 2010 High-speed cycloid-scan atomic force microscopy *Nanotechnology* **21** 365503
[34] Zhang K, Herrmann G, Edwards C, Burgess S C and Miles M J 2014 A non-raster scanning approach in atomic force microscopy using a combined contour prediction algorithm *Proc. 19th World Congress of the Int. Federation of Automatic Control (Cape Town, 24–29 August)* vol **19** pp 5908–13